Article

Polymorphism in AB Nanoparticle Superlattices: An Example of Semiconductor–Metal Metamaterials

Elena V. Shevchenko, Dmitri V. Talapin, Stephen O'Brien, and Christopher B. Murray

J. Am. Chem. Soc., **2005**, 127 (24), 8741-8747• DOI: 10.1021/ja050510z • Publication Date (Web): 27 May 2005

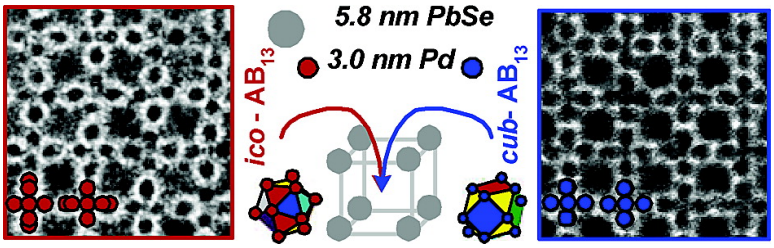

More About This Article

Additional resources and features associated with this article are available within the HTML version:

- Supporting Information
- Links to the 20 articles that cite this article, as of the time of this article download
- Access to high resolution figures
- Links to articles and content related to this article
- Copyright permission to reproduce figures and/or text from this article

View the Full Text HTML

J|A|C|S
ARTICLES
Published on Web 05/27/2005

Polymorphism in AB_{13} Nanoparticle Superlattices: An Example of Semiconductor−Metal Metamaterials

Elena V. Shevchenko,*,†,‡ Dmitri V. Talapin,† Stephen O'Brien,‡ and Christopher B. Murray†

Contribution from the IBM T.J. Watson Research Center, Nanoscale Materials and Devices Group, 1101 Kitchawan Road, Yorktown Heights, New York 10598, and Department of Applied Physics & Applied Mathematics, Columbia University, 200 SW Mudd Building, 500 West 120th Street, New York, New York 10027

Received January 25, 2005; E-mail: eshevche@us.ibm.com; cbmurray@us.ibm.com

Abstract: Colloidal crystallization of nanoparticles with different functionalities into multicomponent assemblies provides a route to new classes of ordered nanocomposites with novel properties tunable by the choice of the constituent building blocks. While theories based on hard sphere approximation predict crystallization of only a few stable binary phases (NaCl-, AlB_2- and $NaZn_{13}$-type), we find that additional polymorphs of lower packing density are possible. We demonstrate that PbSe and Pd nanoparticles can be reproducibly crystallized into two polymorphs with AB_{13} stoichiometry. One polymorph is isostructural with the intermetallic compound $NaZn_{13}$ and is consistent with dense packing of hard spheres driven by entropy. The second unanticipated polymorph is of lower packing density. This observation underscores the shortcomings of applying simple space-filling principles to the crystallization of organically passivated nanocrystals and further motivates the development of models that incorporate combinations of hard-sphere, van der Waals, dipolar, and hydrophobic forces. This work demonstrates that ordered periodic structures with lower packing density are achievable and provides the first example of a binary semiconductor−metal superlattice using a combination of PbSe−Pd nanocrystals.

Introduction

Colloidal synthetic methods now produce nanoparticles with precisely controllable size and shape.[1−5] These nanoparticle systems provide a set of "building blocks" for the assembly of two- and three-dimensional nanoparticle arrays with properties of both fundamental and practical interest.[6−10] Assembling two different types of nanoparticles in a single material not only combines the properties of the building blocks but provides model systems with which to explore the development of new collective properties that may emerge from nanoparticle interactions. For example, the combinations of two different magnentic materials (one with high coercivity and the other with high magnetic moment) can produce higher energy density magnets,[11] while semiconductor and magnetic composites might be explored for magnetooptics. Ordered films of multicomponent mixtures could also be valuable as multifunctional catalysts or photocatalysts.

Crystallization of two different nanoparticle samples into long-range ordered solids by drop-casting requires precise control of particle size, monodispersity, and capping ligands in addition to careful selection of the dispersing solvent and adjustment of the temperature affecting the rate of solvent evaporation. Several examples of colloidal binary superstructures isostructural with intermetallic alloys such as AlB_2,[12,13] $CaCu_5$,[12,14] $NaZn_{13}$,[12] and NaCl[15] have recently been demonstrated. Calculations based on hard sphere approximation predict only three stable phases (e.g. NaCl, AlB_2, and $NaZn_{13}$).[16,17] The $NaZn_{13}$ structure (space group *Fm*3*c*, 226) with its unit cell of eight large and 104 small particles is used as a model system in many theoretical calculations, making it an ideal system for experimental study of nanoparticle superlattices. $NaZn_{13}$ and several homologous AB_{13} intermetallic compounds, such as KZn_{13} and

† IBM.
‡ Columbia University.

(1) Sun, S.; Murray, C. B.; Weller, D., Folks, L.; Moser, A. *Science* **2000**, *287*, 1989−1992.
(2) Milliron, D. J.; Hughes, S. M.; Cui, Y.; Manna, L.; Li, J.; Wang, L.-W.; Alivisatos, A. P. *Nature* **2004**, *430*, 190−195.
(3) Talapin, D. V.; Rogach, A. L.; Kornowski, A.; Haase, M.; Weller, H. *Nano Lett.* **2001**, *1*, 207−211.
(4) Dumestre, F.; Chaudret, B.; Amiens, C.; Renaud, P.; Fejes, P. *Science* **2004**, *303*, 821−823.
(5) Hines, M. A.; Guyot-Sionnest, P. *J. Phys. Chem.* **1996**, *100*, 468−471.
(6) Murray, C. B.; Kagan, C. R.; Bawendi, M. G. *Annu. Rev. Mater. Sci.* **2000**, *30*, 545−610.
(7) Rogach, A. L.; Talapin, D. V.; Shevchenko, E. V.; Kornowski, A.; Weller H. *Adv. Funct. Mater.* **2002**, *12*, 653−664.
(8) Wang, Z. L. *Adv. Mater.* **1998**, *10*, 13−30.
(9) Doty, R. C.; Yu, H.; Shih, C. K.; Korgel, B. A. *J. Phys. Chem. B* **2001**, *105*, 8291−8296.
(10) Talapin, D. V.; Shevchenko, E. V.; Murray, C. B.; Kornowski, A.; Forster, S.; Weller, H. *J. Am. Chem. Soc.* **2002**, *126*, 12984−12988.
(11) Zeng, H.; Li, J.; Liu, J. P.; Wang, Z. L.; Sun, S. *Nature* **2002**, *420*, 395−398.
(12) Redl, F. X.; Cho, K.-S.; Murray, C. B.; O'Brien, S. *Nature* **2003**, *423*, 968−970.
(13) Kiely, C. J.; Fink, J.; Brust, M.; Bethel, D.; Schiffrin, D. J. *Nature* **1998**, *396*, 444−446.
(14) Shevchenko, E. V.; Talapin, D. V.; Rogach, A. L.; Kornowski, A.; Haase, M.; Weller, H. *J. Am. Chem. Soc.* **2002**, *124*, 11480−11485.
(15) Saunders, A. E.; Korgel, B. A. *ChemPhysChem* **2005**, *6*, 61−65.
(16) Cottin, X.; Monson, P. A. *J. Chem. Phys.* **1995**, *102*, 3354−3360.
(17) Trizac E.; Eldridge, M. D.; Madden, P. A. *Mol. Phys.* **1997**, *90*, 675−678.

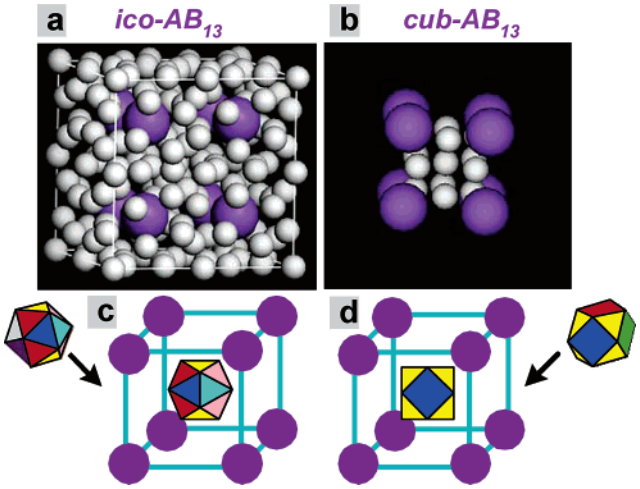

Figure 1. Unit cells of (a) *ico*-AB_{13} and (b) *cub*-AB_{13} superlattice. Large violet A and small gray B spheres represent PbSe and Pd nanoparticles, respectively. (c) subcell of icosahedral AB_{13} ($NaZn_{13}$ type structure) and (d) unit cell of cuboctahedral AB_{13} are depicted. The 12 small B spheres are arranged around the central B atom at the vertexes of (c) a slightly distorted icosahedron and (d) cuboctahedron.

KCd_{13}, were identified almost 70 years ago.[18] Although the AB_{13} structures have been extensively investigated, this icosahedral form of AB_{13} ($NaZn_{13}$-type, further referred to as *ico*-AB_{13}) had been the only structure with AB_{13} stoichiometry that has been reported for either intermetallic compounds or colloidal crystal systems.[19−22] In these structures a small sphere B is surrounded by 12 other B spheres, each at the vertexes of a slightly distorted *icosahedron*, while each large sphere A is surrounded in turn by 24 B spheres at the vertexes of a snub cube[18] (Figure 1a,c).

Our studies of AB_{13} nanoparticle binary assemblies reveal that an additional phase of lower density can form. We identify an alternative organization of small B particles within the AB_{13} superlattices, where B spheres occupy the vertexes of *cuboctahedron*, forming the dense cuboctahedral shell around the central B sphere (Figure 1b,d). This structure will hereafter be referred to as *cub*-AB_{13}. The *cub*-AB_{13} form was considered a possible solution to colloidal AB_{13} packing in early work[19] but was rejected as improbable as it has lower density than the *ico*-AB_{13} form. To our knowledge, *cub*-AB_{13} has not been identified experimentally in either intermetallic compounds or in colloidal binary superstructures. The *ico*-AB_{13} and *cub*-AB_{13} polymorphs differ in the organization of the small B nanoparticles

Hard sphere approximation work well for calculating the properties of colloidal systems such as latex spheres and silica particles. Such calculations provide insights into fundamental nucleation phenomena and crystal growth,[23−29] but they cannot fully describe the assembly of organically stabilized nanoparticles. Our organically stabilized semiconductor and metallic nanoparticles are not simple hard spheres, as they interact via more complex interparticle potentials (a combination of van der Waals and dipolar forces, and they contribute hydrophobic interactions). By varying the solvent salt concentration or by applying external electric fields, the colloidal interaction can be tuned from hard sphere to soft and dipolar in character, allowing richer organization.[30] It is not remarkable that the simple theories do not extend to explain our results; however, our studies show that these more complex interactions can direct the formation of well-crystallized but less dense phases.

Table 1. Calculated Packing Density and the Range of Stability of Hard Sphere AB_{13} Lattice

structure	maximum packing density	size ratio (γ) for maximum packing density	range of stability	ref
ico-AB_{13}	0.738	0.58	$0.54 \le \gamma \le 0.61$	16
			$0.474 \le \gamma \le 0.626$	31
ico-AB_{13}, with some size distribution for B spheres	0.760	0.565	$0.537 \le \gamma \le 0.583$	19
cub-AB_{13}	0.700	0.565	not stable	19

Results and Discussion

Theoretical calculations[16,31,32] confirm the stability of *ico*-AB_{13} structure in mixtures of *hard spheres.* The range of size ratios ($\gamma = R_{small}/R_{large}$) over which *ico*-$AB_{13}$ superlattices are predicted to be stable depends the method of calculation (Table 1). Monte Carlo simulations[31] demonstrated that no specific energetic interactions are needed to stabilize such a complex structure with 112 spheres per cell, but rather the formation can be supported by entropic effects alone: the entropy of *ico*-AB_{13} in a certain A-to-B size ratio is higher than the entropy of a mixture of *fcc* single-component supercrystals.

The majority of theories applied to this field utilize the *hard sphere* approximation, assuming that the particles do not feel each other's presence until their physical surfaces come into contact. Although the results of such calculations are interesting and undoubtedly useful for a wide range of colloidal systems, they cannot fully describe the assembly of nanoparticles comprising a hard core surrounded by soft organic shell that interact through a combination of van der Waals and dipolar forces. Also capping molecules can themselves contribute interactions between nanoparticles or between nanoparticles and substrate.

In this work, we focus on examples of the AB_{13} superlattices formed by 5.8-nm PbSe and 3.0-nm Pd nanoparticles, stabilized by oleic acid and dodecanethiol, respectively (Figure 2). In both cases, the particles are faceted crystals but can be roughly approximated by a sphere. The standard deviation of nanoparticle diameters was determined to be 5% and 7% for PbSe and Pd, respectively. Distributions were determined by image analysis of large field of view transmission electron microscopy (TEM) images and thus set an upper bound on the dispersion as the software convolutes the faceted shapes with the actual distribution of particle dimensions. The significant difference

(18) Shoemakker, D.; Marsh, R.; Ewing, F.; Pauling, L. *Acta Crystallogr*. **1952**, *5*, 637−644.
(19) Murray, M. J.; Sanders, J. V. *Philos. Mag. A* **1980**, *42*, 721−740.
(20) Bartlett, P.; Ottewill, R. H.; Pusey, P. N. *Phys. Rev. Lett.* **1992**, *68*, 3801−3804.
(21) Sanders, J. V. *Philos. Mag. A* **1980**, *42*, 705−720.
(22) Hachisu, S.; Yoshimura, S. *Nature* **1980**, *283*, 188.
(23) Lekkerkeeker, H. N. W.; Stroobants A. *Nature* **1998**, *393*, 305−307.
(24) Auer, S.; Frenkel, D. *Nature* **2001**, *413*, 711−713.
(25) Martin, S.; Bryant, G.; van Megen, W. *Phys. Rev E* **2003**, *67*, 061405-1−061405-11.
(26) Mau, S.-C.; Huse, D. A. *Phys. Rev E* **1999**, *59*, 4396−4401.
(27) Kaplan, P. D.; Rouke, J. L.; Yodh, A. G.; Pine, D. J. *Phys. Rev. Lett.* **1994**, *72*, 582−585.
(28) Auer, S.; Frenkel, D. *Phys. Rev. Lett.* **2003**, *91*, 015703-1−015703-4.
(29) Nunt, N.; Jardine, R.; Partlett, P. *Phys. Rev E* **2000**, *62*, 900−913.
(30) Yethraj, A.; van Blaaderen, A. *Nature* **2003**, *421*, 513−517.
(31) Eldridge, M. D.; Madden, P. A.; Frenkel D. *Nature* **1993**, *365*, 35−37.
(32) Eldridge, M. D.; Madden, P. A.; Frenkel, D. *Mol. Phys.* **1993**, *79*, 105−120.

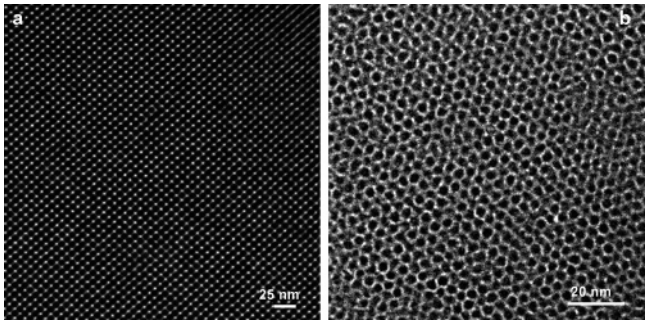

Figure 2. TEM overview of 3D superlattices, formed by (a) 5.8-nm PbSe and (b) 3.0-nm Pd nanoparticles under conditions used to grow AB_{13} superlatties.

in density and compressibility of inorganic core and organic shell leads to uncertainty in defining the effective nanoparticle size. The effective thicknesses of dodecanethiol and oleic acid shells were determined by TEM measurements of average interparticle distances in two-dimensional (2D) arrays of single component Pd and PbSe nanoparticles. The light organic groups are transparent to the electron beam and the light regions represent the measure of separation between the hard inorganic cores of nanoparticles. Dodecanethiol forms a 0.85-nm-thick shell around the 3.0-nm Pd core, which is in good agreement with the calculated *effective* thickness of this capping ligand.[33] The effective thickness of the oleic acid shell around the 5.8-nm PbSe nanoparticles was also found to be about 0.85 nm. The interparticle distance is influenced by the chain length of capping molecules; however, interdigitation of chains generally reduces the spacing between nanoparticles to significantly less than the extended length of an individual molecule. The similar interparticle distances in the case of 2D layers of PbSe and Pd nanoparticles stabilized by oleic acid (C_{18}) and dodecanethiol (C_{12}), respectively, most likely arise from interdigitation or chain folding.[33] As another possible explanation, only the Pb sites on the surface of PbSe are expected to be coordinated by oleic acid, leading to a less dense organic coat than that on the Pd, where each surface atom might bind a thiol group.

When using PbSe and Pd particles with the effective size ratio of 0.627 (including the ligand shells), which is close to the upper limit of γ calculated for stable *ico*-AB_{13} (Table 1), two types of AB_{13} superlattice are identified: (i) the expected *ico*-AB_{13} (Figure 3a,c) and (ii) the new AB_{13} polymorph (*cub*-AB_{13}) (Figure 1b,d). Figure 3a shows the TEM of a $[100]_{sl}$ (subscript "sl" denotes superlattice) projection of two polymorphous forms of AB_{13}. In this sample, the fragments of *ico*-AB_{13} (circled in red, Figure 3a) are smoothly transformed into *cub*-AB_{13} phase (circled in blue, Figure 3a). Parts b and c of Figure 3 illustrate the [100] projections of the subcells of modeled *ico*-AB_{13} and *cub*-AB_{13} superlattices, correspondingly. Parts a and b of Figure 4 show TEM images of a superlattice of 3.0-nm Pd and 5.8-nm PbSe nanoparticles, which match the $[100]_{sl}$ and $[110]_{sl}$ planes of the modeled *ico*-AB_{13} (cf. Figure 4, parts a,c and b,e). The neighboring subcells in the *ico*-AB_{13} lattice have icosahedrons rotated by 90°. This alternating orientation of icosahedra can be seen in the TEM image (Figure 4a). The full unit cell of *ico*-AB_{13} contains eight subcells or 112 atoms (Figure 1a). The alternating arrangement of icosahedra provides the highest packing density for this type of superlattice. On the other hand, the cuboctahedra in *cub*-AB_{13} lattice have the same orientation, and the full unit cell of *cub*-AB_{12} contains only 14 atoms.

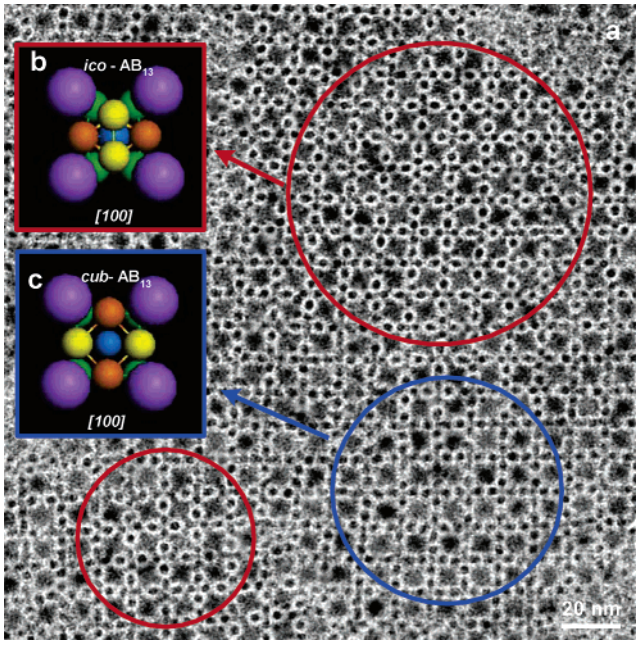

Figure 3. (a) TEM overview of $[100]_{sl}$ planes of *cub*-AB_{13} (area in blue circle) and *ico*-AB_{13} (areas in read circles); depiction of [100] planes of (b) *ico*-AB_{13}, and (c) *cub*-AB_{13}: large violet spheres indicate large A spheres. Differently colored small spheres visualize the arrangement of 12 small B spheres at the vertexes of cuboctahedron and at the vertexes of slightly distorted icosahedron, respectively, around the central B atom (colored in blue).

Since an icosahedron is a distorted form of a cuboctahedron,[34] small particles can also occupy the vertexes of a cuboctahedron instead of occupying the vertexes of icosahedron (Figure 1, parts b,d and a,c). The cuboctahedral shell around the central particle is characteristic for the cubic close-packed (ccp) structures.[34,35] Figure 1b represents the model of AB_{13} crystalline structure with cuboctahedral organization of small particles (*cub*-AB_{13}). Parts a and b of Figure 5 show TEM images of a superlattice of 3.0-nm Pd and 5.8-nm PbSe nanoparticles, which match the $[100]_{sl}$ and $[110]_{sl}$ planes of the modeled *cub*-AB_{13} (cf. Figure 5, parts a,c and b,e).

The layer-by-layer modeling of different projections of *ico*-AB_{13} and *cub*-AB_{13} superstructures allows us to estimate the minimum number of nanoparticle layers (Figures 4d,f and 5d,f) needed to form the patterns observed in TEM. Although thicker regions grow in each sample, these areas are not sufficiently electron transparent for our analysis.

Sanders and Murray[19] stated that this cuboctahedral organization of spheres could take place under the influence of van der Waals' forces because of a larger number of particle−particle contacts per unit cell, which can minimize the energy of structure. However, *ico*-AB_{13} is expected to be favored, due to its higher calculated packing density (0.738) as compared with *cub*-AB_{13} (0.700). Moreover, in the case of *ico*-AB_{13}, the number of interparticle contacts can be increased by a slight deviation from an ideal icosahedron.[19]

(33) Korgel, B. A.; Fullam, S.; Connolly, S.; Fitzmaurice, D. *J. Phys. Chem. B* **1998**, *102*, 8379−8388.
(34) Mackay, A. L. *Acta Crystallogr.* **1962**, *15*, 916−918.
(35) Aslanov, L. A. *Acta Crystallogr.* **1998**, *B44*, 449−458.

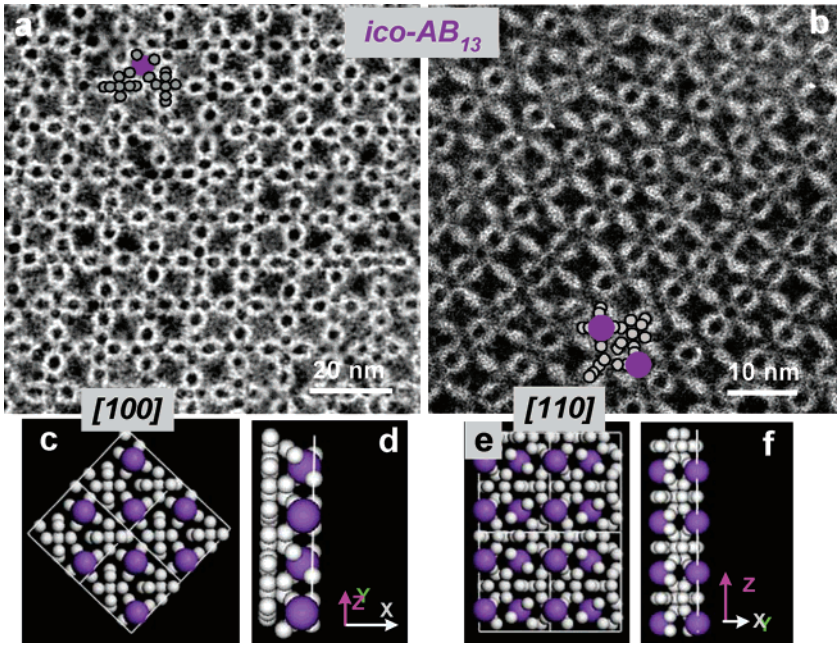

Figure 4. TEM micrographs of (a) $[100]_{sl}$ and (b) $[110]_{sl}$ projections of *ico*-AB_{13} superlattices; depictions of (c) [100] and (e) [110] planes of *ico*-AB_{13} superlattices; depictions of minimum number of layers in (d) [100] and (f) [110] planes of *ico*-AB_{13}, leading to the formation of structures equivalent to the observed ones.

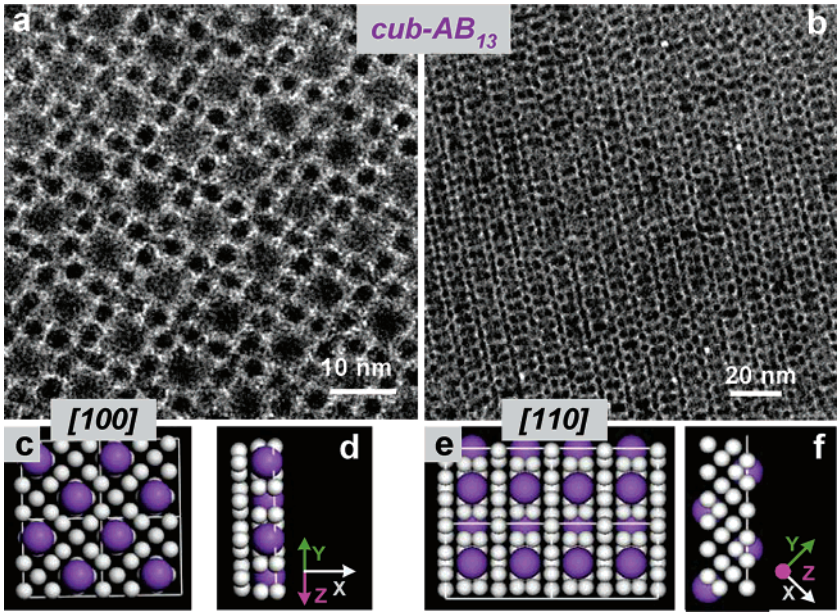

Figure 5. TEM micrographs of (a) $[100]_{sl}$ and (b) $[110]_{sl}$ projections of *cub*-AB_{13} superlattices; depictions of (c) [100] and (e) [110] planes of *cub*-AB_{13} superlattices; depictions of minimum number of layers in (d) [100] and (f) [110] planes of *cub*-AB_{13}, leading to the formation of structures equivalent to the observed ones.

The probability of formation of a given binary structure can be calculated by comparing the entropy of a binary structure with the entropy of single-phase superlattices. For example, Frenkel et al. demonstrated that a $NaZn_{13}$-type superlattice can form because of the high entropy of this structure compared to a phase-separated mixture of fcc crystals.[31] However, if detailed entropy calculations are not available, simple hard sphere packing arguments suggest that binary assemblies can be stable if their packing density exceeds the packing density of single-component crystals in a fcc or hcp structure (~0.7405).[19] In fact, in the case of *ico*-AB_{13}, a finite size distribution among the smaller particles can lead to an increase of the packing density. For instance, a slightly smaller sphere inside the icosahedron (the size of central sphere is ~90% of the size of particles at the vertexes of icosahedron) gives rise to a packing density up to 0.76.[19] However, in the case of *cub*-AB_{13}, such a size distribution is expected to further reduce its stability, as it leads to the formation of even more open structures.[19] As mentioned above, both PbSe and Pd nanoparticles have some residual size distribution which should, in principle, increase the probability of the formation of *ico*-AB_{13}. Nevertheless, our experimental results on crystallization of nanoparticles in binary mixtures indicate that *cub*-AB_{13} can coexist with *ico*-AB_{13}, despite the low calculated maximum packing density. The shape of particles may also affect the packing density of both AB_{13} forms.[19]

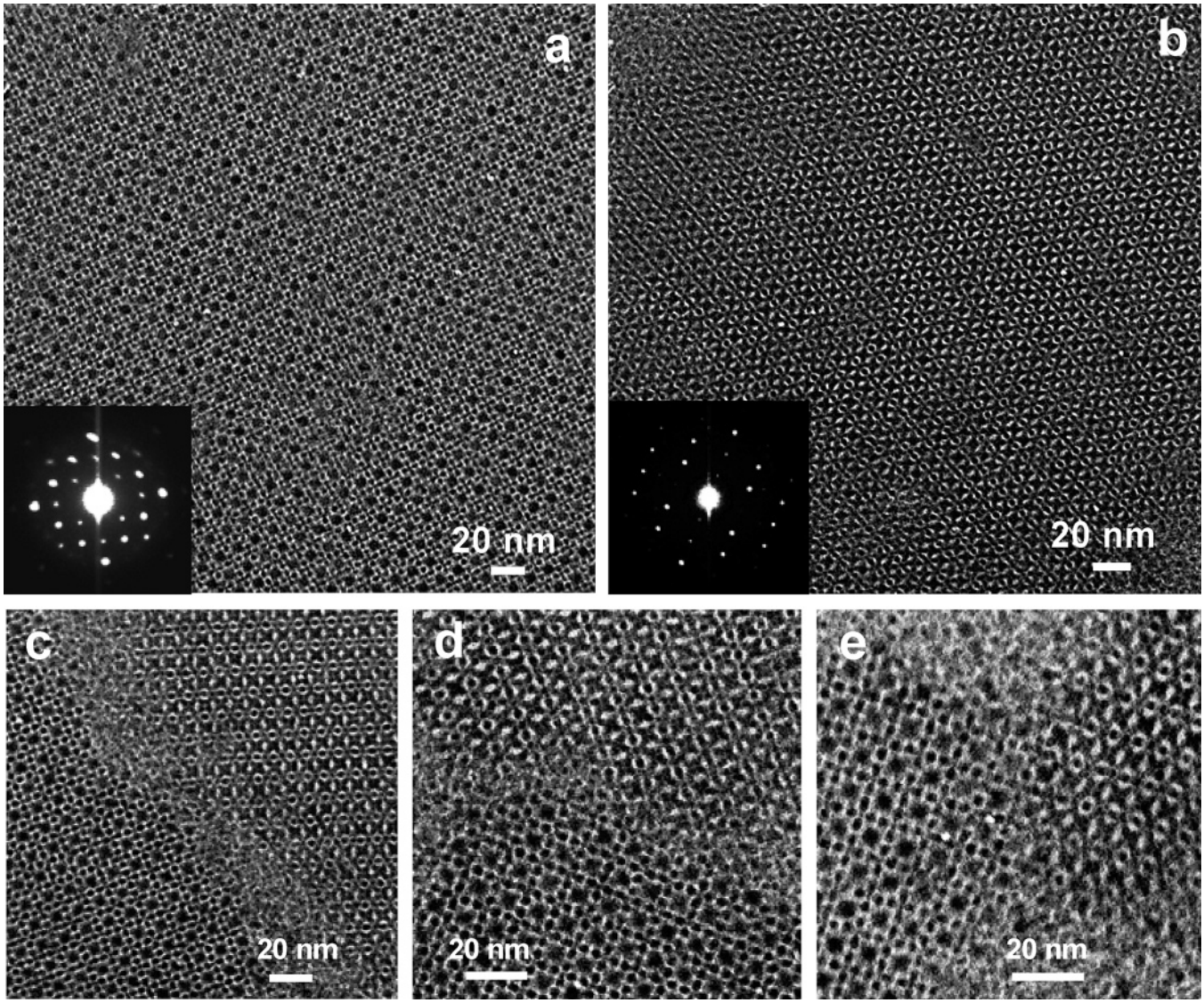

Figure 6. TEM overviews and small-angle electron diffraction patterns from ~1 μm^2 areas of (a) $[100]_{sl}$ projections of *cub*-AB_{13} and (b) $[110]_{sl}$ projections of *ico*-AB_{13} superlattices. TEM images (c−e) demonstrating the coexistence of the domains with *ico*- and *cub*-AB_{13} ordering.

The alternating arrangement of icosahedra in the neighboring subcells of the *ico*-AB_{13} lattice results in a unit cell consisting of eight subcells with 112 spheres per unit cell. The stability of this complex structure is due to its high packing density and high entropy. On the other hand, the unit cell of *cub*-AB_{13} lattice contains only 14 spheres and has higher internal symmetry. Comparison of stability of these lattices predicts favorable formation of *ico*-AB_{13}[19] while our experiments show that both structures can form. Although *ico*-AB_{13} is thermodynamically more stable, we assume that the simpler structure of the *cub*-AB_{13} lattice can more easily nucleate and grow under kinetic control. Formation of different types of AB_{13} superlattices can occur as interplay between thermodynamic and kinetic factors.

In addition to offering different densities, these two polymorphs allow engineering of the superlattice orientation. Surveys of many samples show a strong tendency for *ico*-AB_{13} structures to orient with the $[110]_{sl}$ planes (Figures 4b and 6b) parallel to the substrate, while only small fragments of $[110]_{sl}$ planes of *cub*-AB_{13} (Figure 5b) can be found on the substrates. In contrast, $[100]_{sl}$ orientation dominates for the *cub*-AB_{13} regions. Ordered $[100]_{sl}$ planes of *cub*-AB_{13} and $[110]_{sl}$ planes of *ico*-AB_{13} are typically in the range of 0.2−2 μm across an edge (Figure 6a,b). The symmetry of each projection is confirmed by fast Fourier transform (FFT) of the TEM images in addition to the small-angle electron diffraction patterns from the areas of ~1−4 μm (Figure 6a,b, insets). The preferential growth of certain crystallographic directions on the substrate is still an open question, even in the case of superlattices of monodisperse nanoparticles. A recent study by Sigman et al. demonstrates that Au and Ag nanoparticles stabilized by dodecanethiol form fcc superlattice oriented with $(111)_{s1}$ planes parallel to the substrate.[36] In the case of monodisperse PbSe and Pd nanoparticulate superlattices, the contribution of $(111)_{sl}$-oriented planes was also high. However, the other planes (e.g., $(100)_{sl}$, $(101)_{s1}$) parallel to the substrate can be also easily detected, especially in the case of PbSe nanoparticles.[37] Both $(111)_{sl}$- and $(100)_{sl}$-oriented colloidal CdSe crystals can be formed from the same sample preparation.[6] In the case of binary superlattices isostructural with NaCl and

(36) Sigman, M. B.; Saunders: A. E.; Korgel, B. A. *Langmuir* **2004**, *20*, 978−983.
(37) Chen, F.; Stokes, K. L.; Zhou, W.; Fang, J.; Murray, C. B. *Mater. Res. Soc. Symp. Proc.* **2002**, *691*, G10.2.1−G10.2.6.

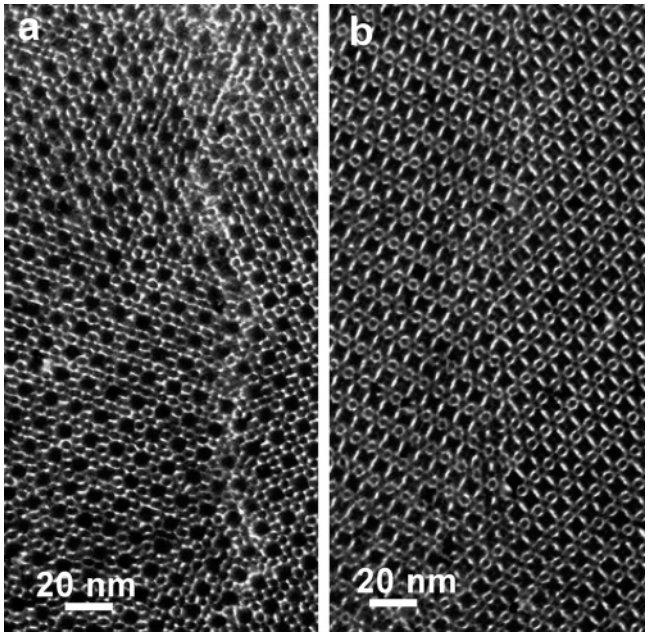

Figure 7. TEM micrographs of the plane defects in AB_{13} superlattices, representing stacking faults in (a) $[100]_{sl}$ plane of *cub*-AB_{13} and (b) $[110]_{sl}$ plane of *ico*-AB_{13} superlattices.

AlB_2, different planes form simultaneously on the substrate.[15,17] The relatively short period that binary superlattices have been under study makes us reluctant to draw more universal conclusions yet about the crystallization mechanisms. We would, however, speculate that, in the case of AB_{13} polymorphs, the growth of *cub*-AB_{13} and *ico*-AB_{13} with $[100]_{sl}$ and $[110]_{s1}$ preferential orientation may be due to the alignment of the facets of the icosahedron and cuboctahedron of small particles with the plane of the substrate.

The domains of *ico*-AB_{13} and of *cub*-AB_{13} superlattices are often separated by thin "amorphous" bands (Figure 6c) or by grain boundaries (Figure 6d), although smooth transitions between *ico*-AB_{13} and *cub*-AB_{13} domains can also be observed (Figures 3a and 6e), indicating that only subtle differences in energy might exist. In both types of AB_{13} superlattice, the individual nanoparticles are not preferentially oriented with respect to the superlattice. This is consistent with the particle shape being near spherical, allowing them to sit rotationally disordered on the superlattice sites. As in atomic or molecular crystals, nanoparticle superlattices possess imperfections. Analysis of multiple TEM images indicate that most imperfections can be attributed to defects, such as dislocations, grain boundaries, and stacking faults (Figure 7).

Trends observed in symmetry and orientation of superlattice growth from 5.8-nm PbSe and 3.0-nm Pd are readily extended to other nanoparticle combinations: 5.3-nm PbSe/3.0-nm Pd nanoparticles ($\gamma \sim 0.671$), 6.2-nm PbSe/3.0-nm Pd nanoparticles ($\gamma \sim 0.595$), and 13.4-nm Fe_2O_3/6.2-nm PbSe nanoparticles ($\gamma \sim 0.520$) (Figure 8). It is worth noting that the effective size ratio of 5.3-nm PbSe and 3.0-nm Pd nanoparticles is far above the calculated stability range of AB_{13} superlattice (Table 1), yet ordering up to micrometer scale is observed.

Conclusions

In our study, two polymorphs of AB_{13} nanoparticle superlattices are grown and characterized. These two phases differ

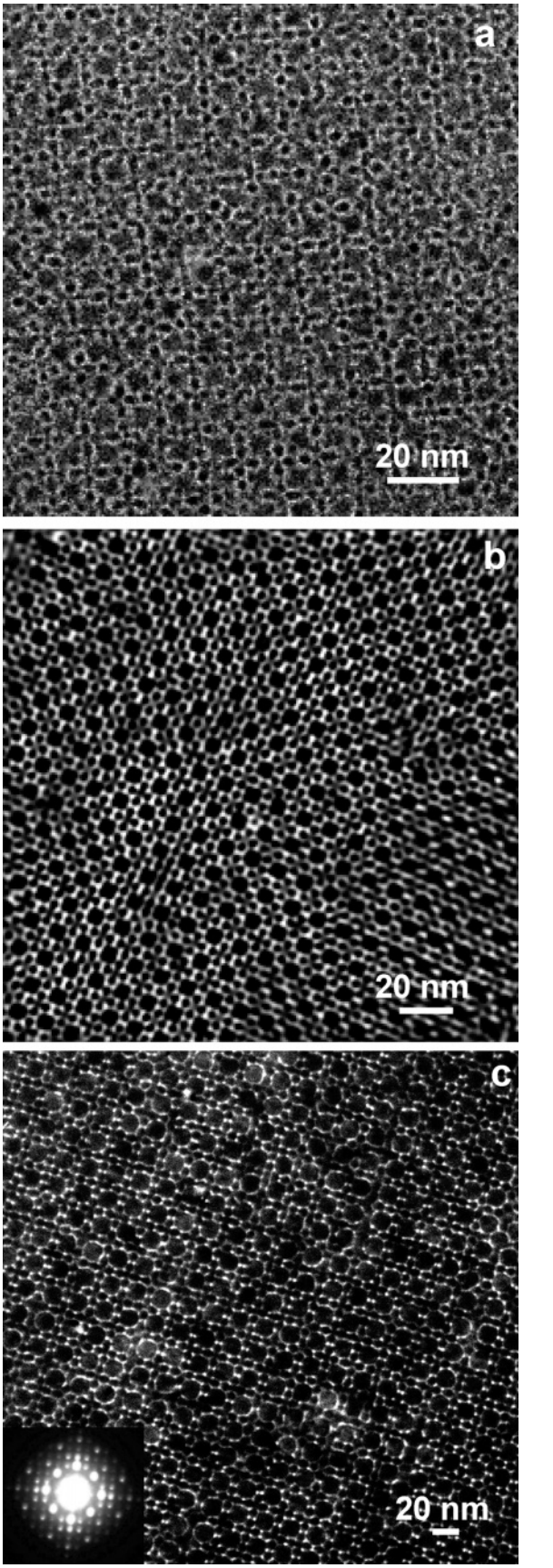

Figure 8. TEM overviews of (a) $[100]_{sl}$ projections of *ico*-AB_{13} consisting of 5.3-nm PbSe and 3.0-nm Pd nanoparticles; (b) $[100]_{sl}$ projections of *cub*-AB_{13} consisting of 6.2-nm PbSe and 3.0-nm Pd nanoparticles and (c) 13.4-nm γ-Fe_2O_3 and 6.2-nm PbSe (inset: small angle electron diffraction pattern).

in their arrangement of smaller B particles, in their density, and in their tendency for the superlattices to orient with respect to the substrate during growth. Small particles occupy either the vertexes of icosahedra or the vertexes of cuboctahedron forming *ico*-AB_{13} (isostructural with $NaZn_{13}$) or *cub*-AB_{13} forms, respectively. The driving forces of the formation of low-density *cub*-AB_{13} superlattice, though unclear, point to the importance of van der Waals and other "non-hard-sphere" interactions between nanoparticles. The contribution of capping molecules in the formation of superlattices also is significant. We have shown that particles with these flexible "soft" organic shells can form binary superlattices over a wider range of size ratios than previously anticipated for hard spheres. The *cub*-AB_{13} domains grow preferentially on the substrates with $[100]_{sl}$ orientation, while the *ico*-AB_{13} domains are $[110]_{sl}$-oriented (Figure 6a,b). The AB_{13} superlattice system emphasized in our study is formed from PbSe and Pd nanoparticles, providing the first example of a binary semiconductor−metal superlattice (metamaterial).

Our observation of two coexisting nanoparticle superlattices with the same stoichiometry but different packing density suggests that the other nondense packed structures can be achievable. This motivates further experimental and theoretical studies to realize and expand a set of binary phases and new nanoparticle combinations.

Experimental Section

Preparation of Pd Nanoparticles. To prepare 3.0-nm Pd nanoparticles, we use a modification of the method, developed for Au and reported in ref 38. In a typical synthesis, 0.0237 g of $PdCl_2$ is dissolved in 10 mL of toluene solution of 0.157 g of didodecyldimethylammonium bromide (DDAB), which is ultrasonicated to provide thorough mixing. Next, 4 μL of 9.4 M aqueous solution of $NaBH_4$ is added dropwise with vigorous stirring. The color of the solutions turns dark brown in the first 5 min. After 20 min of stirring, 1-dodecanthiol is added to the reaction mixture. The metal particles can then be isolated from the DDAB, excess dodecanethiol, and reaction side products by the precipitation with ethanol and centrifugation. The Pd particles are dried under vacuum and redispersed in toluene in the presence of 1-dodecanethiol and refluxed for 30 min under a nitrogen flow. Finally, excess dodecanethiol is removed by precipitating the particles with 2-propanol and redispersing in toluene.

Preparation of PbSe Nanoparticles. For synthesis of 5.8-nm PbSe nanocrystals, 2.16 g of lead acetate trihydrate and 7.3 mL of oleic acid are dissolved in 40 mL of squalane.[39] This mixture is heated to 100 °C for 1 h under vaccum to form lead oleate and to dry the solution. Then, the lead oleate solution is heated to 170 °C, and 18 mL of a 1 M solution of TOPSe in TOP is swiftly injected under vigorous stirring. The reaction mixture is kept at 155−160 °C for 3 min and then promptly cooled to room temperature. A hexane/ethanol (1:3 by volume) mixture is added to the crude solution to precipitate PbSe nanocrystals and remove byproducts.

The γ-Fe_2O_3 nanoparticles were prepared using the approach developed by T. Hyeon et al.[40] Injection of $Fe(CO)_5$ was performed at 220 °C.

Preparation of AB_{13} Superlattices. At room temperature, Pd nanoparticles have a tendency to form aggregates. Heating the toluene solution of Pd nanoparticles improves their solubility. Crystallization of large PbSe and small Pd nanoparticles into AB_{13} superstructures is achieved by evaporation of a toluene dispersion containing 20-fold excess of Pd particles under reduced pressure (∼3.2 kPa) at 45−50 °C. The evaporation of toluene binary mixture at ambient conditions leads to the formation of both forms of AB_{13} superlattices of much smaller dimensions and partial phase segregation of Pd nanoparticles. After crystallization the structures were investigated by TEM (Phillips CM12, operating at 120 kV).

The unit cells of *ico*-AB_{13} and *cub*-AB_{13} superlattices were modeled using Accelrys Software (MS Modeling 3.1) (Figure 3a,b) and cleaved along different crystallographic directions (Figures 4c,e and 5c,e).

Acknowledgment. This work was supported primarily by the MRSEC Program of the National Science Foundation under Award Number DMR-0213574 and by the New York State Office of Science, Technology and Academic Research (NYSTAR). We thank Maxim Sviridenko and Nikhil Bansal (T.J. Watson Research Center, IBM) and Andrew Schofield (Edinburgh University, UK) for helpful discussions.

JA050510Z

(38) Prasad, B. L. V.; Stoeva, S. I.; Sorensen, C. M.; Klabunde, K. J. *Langmuir* **2002**, *18*, 7515−7520.
(39) Steckel, J. S.; Coe-Sullivan, S.; Bulović, V.; Bawendi, M. G. *Adv. Mater.* **2003**, *15*, 1862−1866.
(40) Hyeon, T.; Lee, S. S.; Park, J.; Chung, Y.; Na, H. B. *J. Am. Chem. Soc.* **2001**, *123*, 12798−12801.